J. Fluid Mech. (2013), *vol.* 714, *pp.* 612–633. © Cambridge University Press 2013
doi:10.1017/jfm.2012.512

Magnetic field driven micro-convection in the Hele-Shaw cell

K. Ērglis[1], A. Tatulcenkov[1], G. Kitenbergs[1], O. Petrichenko[1], F. G. Ergin[2], B. B. Watz[2] and A. Cēbers[1,†]

[1]Department of Theoretical Physics, University of Latvia, Riga, Zellu 8, LV-1002, Latvia

[2]Dantec Dynamics A/S, Tonsbakken 16-18, Skovlunde, 2740, Denmark

(Received 2 March 2012; revised 27 September 2012; accepted 11 October 2012)

Micro-convection caused by ponderomotive forces of the self-magnetic field of a magnetic fluid in the Hele-Shaw cell under the action of a vertical homogeneous magnetic field is studied both experimentally and numerically. It is shown that a non-potential magnetic force at magnetic Rayleigh numbers greater than the critical value causes fingering at the interface between the miscible magnetic and non-magnetic fluids. The threshold value of the magnetic Rayleigh number depends on the smearing of the interface between fluids. Fingering with its subsequent decay due to diffusion of particles significantly increases the mixing at the interface. Velocity and vorticity fields at fingering are determined by particle image velocimetry measurements and qualitatively correspond well to the results of numerical simulations of the micro-convection in the Hele-Shaw cell carried out in the Darcy approximation, which account for ponderomotive forces of the self-magnetic field of the magnetic fluid. Gravity plays an important role at the initial stage of the fingering observed in the experiments.

Key words: Hele-Shaw flows, MHD and electrohydrodynamics, magnetic fluids

1. Introduction

Magnetic-field-driven micro-convection was found in the early 1980s (Maiorov & Cebers 1983) extending the previous work on magnetostatic instabilities of magnetic liquids in the Hele-Shaw cell (Cebers & Maiorov 1980) for miscible fluids. Since the ponderomotive force on the magnetizable fluid is proportional to the concentration of magnetic particles and the local gradient of the magnetic field strength, it is potential only when the concentration and magnetic field strength gradients are collinear. The field strength gradient in a homogeneous applied field results from the self-magnetic field of the liquid. Any concentration perturbations that destroy this collinearity cause the liquid to start to flow. An important issue that is absent in gravitational convection is the dependence of the field gradient on the concentration field. It should be mentioned that the equivalent of the thermal expansion coefficient, which in liquids has an order of magnitude of 10^{-3}, is much larger in this case because of the strong dependence of the magnetization of a liquid on the particle concentration.

In view of these considerations, the theoretical model of the magnetic micro-convection considers the Hele-Shaw flow under the action of the ponderomotive forces

† Email address for correspondence: aceb@tesla.sal.lv

due to the self-magnetic field of the fluid, the equations for the magnetostatic field, and the diffusion equation for the concentration of the magnetic nanoparticles (Cebers 1997). The theoretical analysis shows that there is a threshold value of the critical magnetic field strength determined by the magnetic Rayleigh number.

Later, magnetic-field-driven micro-convection has attracted the interest of researchers both from an experimental and a theoretical point of view. Magnetic-field-driven fingering was observed in micro-channels using the methods of microfluidics (Derec *et al.* 2008) and on the interface of a circular region concentrated by magnetic particles (Wen, Chen & Kuan 2007). The concept of the magnetic-field-driven micro-convection was experimentally studied for the case of the time evolution of gratings of magnetic particles induced by thermophoresis at non-homogeneous illumination of the magnetic colloids (Mezulis & Blums 2005). The theoretical analysis of the last problem was given by Igonin & Cebers (2003).

The theoretical analysis of the growth increments of the fingering instability in the case of plane interface between miscible magnetic and non-magnetic fluids was given by Igonin & Cebers (2003). Numerical analysis of the magnetic-field-driven micro-convection in the frame of the described model was carried out by Chen & Wen (2002). In the work of Chen (2003) the effect of the Korteweg stress was taken into account in the numerical simulation of magnetic micro-convection.

In spite of various efforts, the quantitative information on the main characteristics of the micro-convection that develops is rather poor. Even the occurrence of fluid flow during the formation of the fingers at the interface between two miscible fluids has not yet been confirmed. Here we obtain quantitative information on the micro-flow driven by the self-magnetic field of the magnetic colloid by applying particle image velocimetry (PIV) methods with specially designed algorithms for processing images with poor contrast (Ergin *et al.* 2010). The main obstacles for quantitative comparison with the theoretical analysis and numerical simulations given in the first part of the work are discussed, and it is shown that in spite of small density differences between the magnetic fluid and its solvent gravity plays an important role in the smearing of the concentration distribution, which essentially determines the critical field strength for the development of the magnetic micro-convection. Nevertheless, we illustrate that, in general, the numerical simulation and experimental data are in good qualitative agreement.

2. Mathematical formulation

2.1. *Model*

We consider two miscible fluids where the first is a magnetic fluid and the second is a simple non-magnetic fluid. Fluids are confined in a horizontal Hele-Shaw cell and a magnetic field is applied perpendicular to the cell, the sketch of the cell is shown in figure 1. The viscosities of the fluids are equal. The ponderomotive forces of the non-homogeneous self-magnetic field on the interface between fluids cause fingering instability. Its growth is described by the set of equations, which includes the Darcy equation, the convection–diffusion equation and equations for the magnetostatic field (Cebers 1997; Igonin & Cebers 2003) and reads

$$-\nabla p - \frac{12\eta}{h^2}\boldsymbol{u} - \frac{2M(c)}{h}\nabla\psi_m(c) = 0, \quad \nabla\cdot\boldsymbol{u} = 0, \tag{2.1}$$

$$\frac{\partial c}{\partial t} + (\boldsymbol{u}\cdot\nabla)c = D\nabla^2 c, \tag{2.2}$$

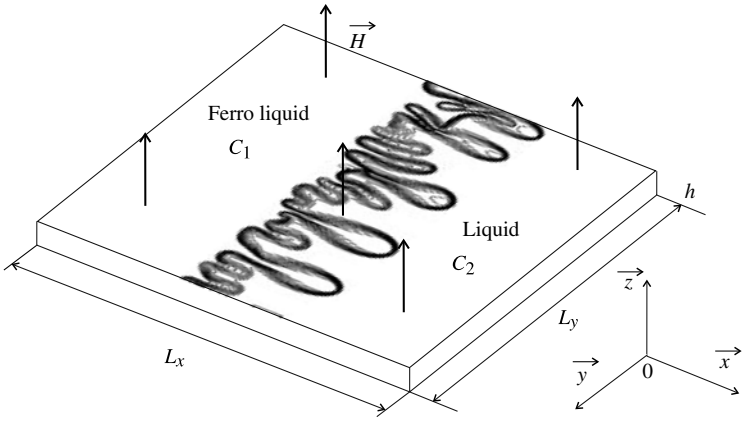

FIGURE 1. The Hele-Shaw cell sketch.

where p is pressure, $\boldsymbol{u} = (u_x(x, y), u_y(x, y))$ is the depth averaged velocity, η is the viscosity of the fluid, h is the thickness of the Hele-Shaw cell, D is isotropic constant diffusion coefficient and c is the concentration of magnetic fluid normalized by its value far from the interface. The magnetization $M(c)$ is taken to be proportional to the concentration of the magnetic fluid c ($M = M_0 c$) and the value of the magnetostatic potential ψ_m on the boundary of the Hele-Shaw cell is given by Cebers (1981) and Jackson, Goldstein & Cebers (1994)

$$\psi_m(\boldsymbol{r}, t) = M_0 \int c(\boldsymbol{r}', t) K(\boldsymbol{r} - \boldsymbol{r}', h)\, \mathrm{d}S', \tag{2.3}$$

where the integration is performed over the boundary of the Hele-Shaw cell, $K(\boldsymbol{r}, h) = 1/|\boldsymbol{r}| - 1/\sqrt{|\boldsymbol{r}|^2 + h^2}$.

Equations (2.1) and (2.2) extend in the Darcy approximation the model which is usually applied for the study of the displacements of miscible, non-magnetic fluids in the Hele-Shaw cell (Goyal & Meiburg 2006).

The boundary conditions for the velocity components and the concentration of the fluid are as follows:

$$u_x(0, y) = u_y(0, y) = 0, \quad c(0, y) = 1, \tag{2.4a}$$

$$u_x(L_x, y) = u_y(L_x, y) = 0, \quad c(L_x, y) = 0, \tag{2.4b}$$

and the conditions of the periodicity across the Hele-Shaw cell are

$$\boldsymbol{u}(x, 0, t) = \boldsymbol{u}(x, L_y, t), \quad c(x, 0, t) = c(x, L_y, t). \tag{2.5}$$

The boundary conditions (2.4) require that the fluid is motionless at both ends of the cell. The motion of the liquid arises from a non-potential magnetic force $-2M(c)\nabla\psi_m/h$.

The equations are put in dimensionless form by introducing the following scales: length h, time h^2/D, velocity D/h and magnetostatic potential $M_0 h$. As a result the set of dimensionless equations reads

$$-\nabla p - \boldsymbol{u} - 2Ra_m c \nabla\psi_m = 0, \quad \nabla \cdot \boldsymbol{u} = 0, \tag{2.6}$$

$$\frac{\partial c}{\partial t} + (\boldsymbol{u} \cdot \nabla) c = \nabla^2 c. \tag{2.7}$$

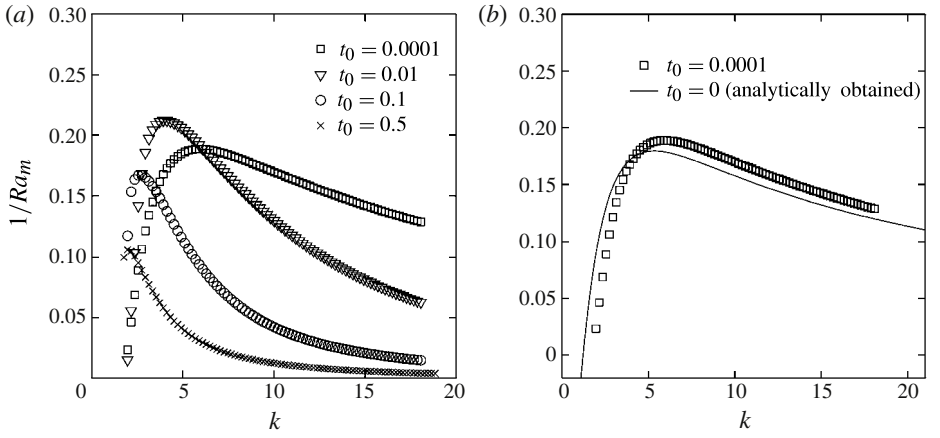

FIGURE 2. (*a*) The neutral curves of the magnetic micro-convection for different values of the smearing parameter ($t_0 = 0.5$, $t_0 = 0.1$, $t_0 = 0.01$, $t_0 = 0.0001$). (*b*) The theoretical neutral curve (solid line) and the neutral curve calculated numerically (dashed line).

Here $Ra_m = M_0^2 h^2/12\eta D$ is the magnetic Rayleigh number determined by the ratio of the characteristic time of the diffusion $\tau_D = h^2/D$ and the characteristic time of motion due to non-homogeneous self-magnetic field of the fluid $\tau_M = 12\eta/M_0^2$.

2.1.1. *The linear stability analysis*

In order to test the numerical algorithm, we compare the theoretical results of a linear stability analysis with the numerical results. The solution of the quasi-steady linear stability problem for miscible magnetic fluid in the Hele-Shaw cell is found in Igonin & Cebers (2003). An analytical solution may be found for the value of the smearing parameter $t_0 = 0$. The linear perturbation of a quiescent base state is represented by $\{v_x, v_y, c, \psi_m\}(x, y, t) = \{0, 0, c_0, \psi_{m0}\}(x) + \{v_x', v_y', c', \psi_m'\}(x)\mathrm{e}^{\mathrm{i}ky+\lambda t}$ ($c_0 = 0.5(1 - \mathrm{erf}(x/2\sqrt{t_0}))$), where the parameter t_0 characterizes the thickness of the interfacial region. We focus on the linear analysis of the stability of the interface in the formal limit $t_0 = 0$ when the concentration distribution is step-like. The dispersion relation reads

$$ks + Ra_m[2\mathrm{J}(s, k) - kf(k(s + 1))] = 0, \tag{2.8}$$

where the parameter s is $s = \sqrt{1 + \lambda/k^2}$ and the functions $\mathrm{J}(p, q)$ and $f(p)$ are defined by the integrals

$$\mathrm{J}(p, q) = \int_0^\infty \mathrm{e}^{-pz}(\mathrm{K}_0(z) - \mathrm{K}_0(\sqrt{z^2 + q^2}))\,\mathrm{d}z, \tag{2.9}$$

$$f(p) = \int_0^\infty \mathrm{e}^{-pz}\ln(1 + z^{-2})\,\mathrm{d}z. \tag{2.10}$$

Here K_0 is the modified Bessel function of the second kind (McDonald function).

Neutral curves shown in figure 2(*a*) are calculated numerically as follows. The Fourier coefficients $\hat{c}_n$ for the concentration field averaged along the x-axis $\langle c'\rangle(y) = \int_{L_x} c'(x, y)\,\mathrm{d}x/L_x = \sum_{n=0}^{N_y}\langle\hat{c}_n(t)\rangle\mathrm{e}^{\mathrm{i}k_n y}$ are fitted by $\langle\hat{c}_n\rangle = \langle\hat{c}_n^0\rangle\mathrm{e}^{\lambda_n t}$, and the growth increments λ_n are found in dependence on the wavenumber k_n. The neutral

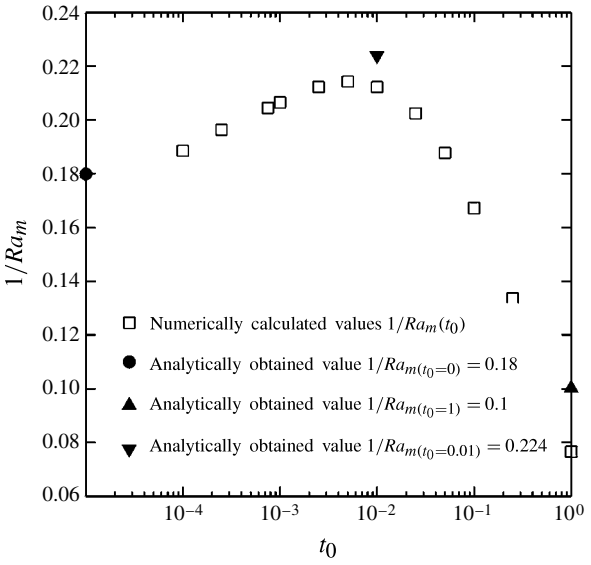

FIGURE 3. The inverse values of the critical magnetic Rayleigh number in dependence on the smearing parameter t_0. Both triangles shown are analytical results from Igonin (2004), and the black circle shows analytical results for the sharp front.

curves for definite values of the smearing parameter t_0 are found by solving the equation $\lambda_n(Ra_m^c, k_n) = 0$ by a spline interpolation.

To reproduce in the simulations growth increments theoretically calculated for a sharp diffusion front it is necessary to take the concentration perturbation corresponding to the theoretically found eigenfunction. The critical values of the magnetic Rayleigh number in dependence on the wavenumber for $t_0 = 0.0001$ with perturbation corresponding to the eigenfunction for a sharp front are shown in figure 2(*b*) by the dashed line. They agree reasonably well with the theoretical values obtained from (2.8) for $t_0 = 0$ and shown in figure 2(*b*) by the solid line. Their small difference is due to difference of eigenfunctions for sharp and smeared fronts.

The inverse values of the critical magnetic Rayleigh number obtained numerically are shown in figure 3 in semi-logarithmic coordinates as a function of t_0. They show agreement with the available theoretical results (Igonin 2004) for sharp and smeared fronts. These tests validate the numerical algorithm.

The numerical algorithm described in appendix A is applied further to study fingering at magnetic micro-convection in the nonlinear regime.

2.2. *Numerical results*

The initial concentration perturbation at the interface is introduced by applying relation (A 6) with $\varsigma(y)$ taken to be random. In long-time numerical calculations typically 512×512 collocation points are used for the space discretization. The time step Δt typically is $\Delta t = 10^{-5}$.

Typical fingering patterns for three values of Ra_m and the smearing parameter $t_0 = 0.05$ are shown in figure 4. The pattern formation has several stages as may be seen in figure 4. At first ($t = 0.0014$ and $t = 0.002$) well-resolved fingers are formed that later coarsen with time ($t = 0.0035$ and $t = 0.009$). Finally, the finger pattern smears out because of diffusion of the magnetic particles ($t = 0.013$).

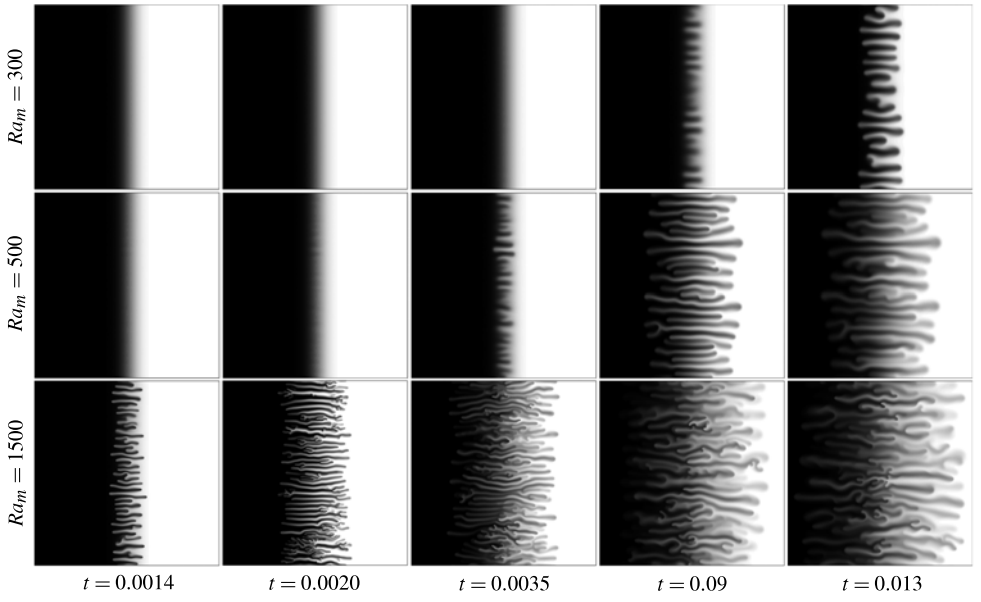

FIGURE 4. Concentration images for magnetic Rayleigh number $Ra_m = 300$, $Ra_m = 500$, $Ra_m = 1500$, at time $t = 0.0014$, $t = 0.002$, $t = 0.0035$, $t = 0.009$, $t = 0.013$, with $L_x = 6$, $L_y = 6$ and $t_0 = 0.05$.

Snapshots of the concentration, vorticity, stream function and velocity fields for $t_0 = 0.05$ and $Ra_m = 500$ at time moment $t = 0.013$ are shown in figure 5. The velocity field is visualized by using the line integral convolution technique. Line integral convolution (LIC) is a powerful technique for generating striking images from vector data and for visualizing vector fields. Introduced by Cabral & Leedom (1993), the method has rapidly found many application areas, ranging from computer art to scientific visualization. Given a vector field and an input texture, line integral convolution produces an output texture in which the data values are highly correlated in the direction of the flow. LIC produces an intensity output image, which is reproduced as a greyscale picture. This image includes tangential information of vector field as well as information on its magnitude. The formation of alternating array of vortices may be seen at figure 5(*b,c*).

To make a qualitative comparison with the experimental data, described in the next part, the time dependence of the maximal vorticity for several values of the magnetic Rayleigh number is calculated and shown in figure 6. The characteristic maximum corresponds to the transition from the development of the magnetic micro-convection to its decay due to particle diffusion. The spiky character of the curve at larger values of the magnetic Rayleigh number is due to the emerging vortices, which intensify the mixing.

3. Experimental demonstration

Magnetic micro-convection is studied on the interface between two miscible fluids. The first fluid is distilled water which contains 0.1 % fluorescent tracer micro-particles with diameter 1 μm for PIV measurements. The second is a water-based magnetic fluid with γ–Fe_2O_3 particles of average radius 14 nm, saturation

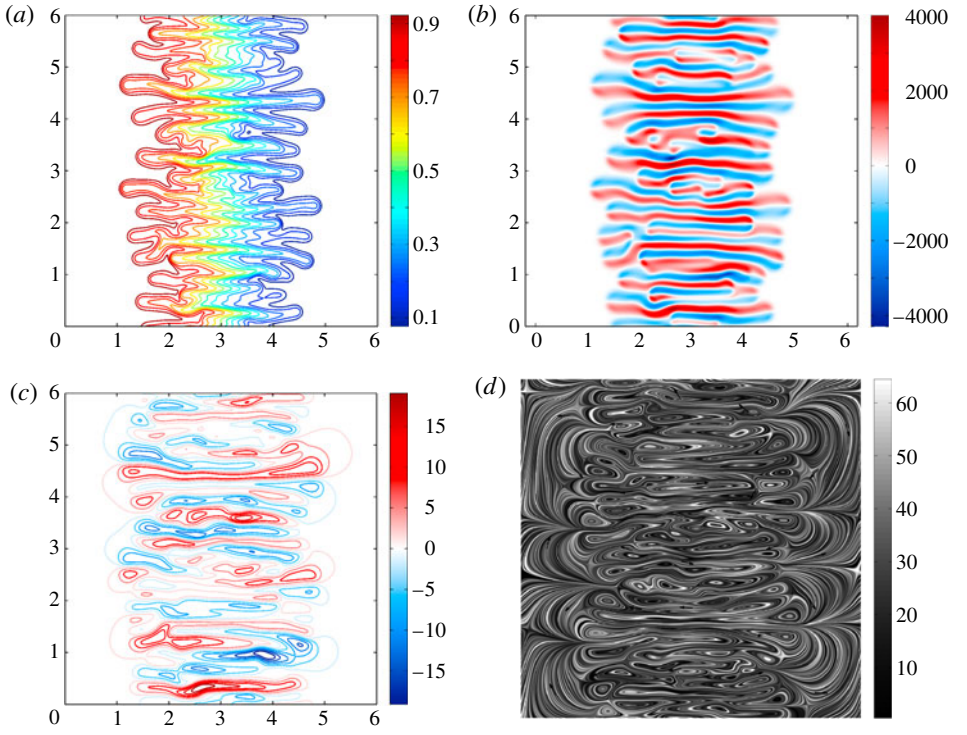

FIGURE 5. Snapshots of concentration (a), vorticity (b), stream function (c) and velocity field (d) for miscible magnetic and non-magnetic fluids in the Hele-Shaw cell. Snapshots correspond to the magnetic Rayleigh number $Ra_m = 500$ at time $t = 0.013$, with $L_x = 6$, $L_y = 6$ and $t_0 = 0.05$.

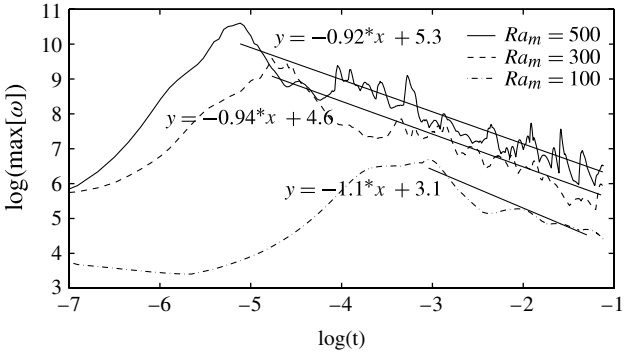

FIGURE 6. The relaxation of the maximal value of vorticity field ω_{max} for different values of magnetic numbers Ra_m on a logarithmic scale.

magnetization 10 G and initial susceptibility 0.064, as determined by the vibrating sample magnetometer measurements. The density of the liquid is $\varrho = 1.077$ g cm^{-3}. The diffusion coefficient of the particles is determined by diffusion light scattering and equals $D = 5.5 \times 10^{-8}$ cm^2 s^{-1}. Magnetic nanoparticles of γ–Fe_2O_3 are synthesized

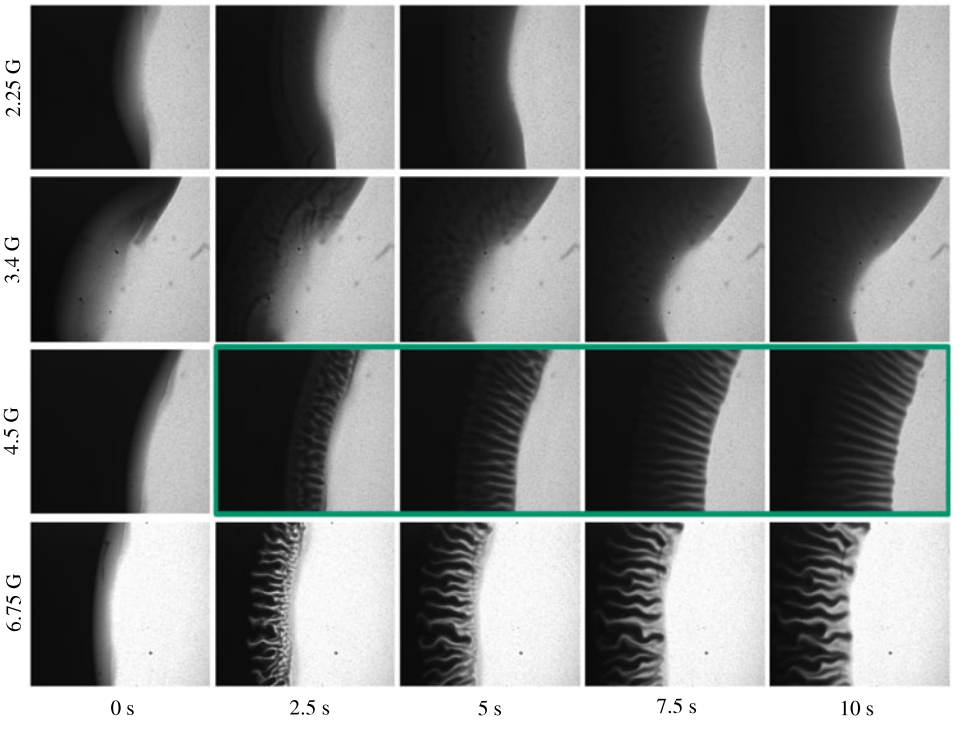

FIGURE 7. Determination of the threshold value of the magnetic field for finger-like pattern development.

by a precipitation reaction (Massart). The Hele-Shaw cell is prepared from two microscope cover glasses separated by a 127 μm thick Parafilm. The Parafilm is cut to form channels for air and fluids. The horizontal dimensions of the fluid channel are 18 mm × 6 mm. After assembly the cell is heated to weld the cover glasses. A few drops of magnetic fluid are placed on one side of the cell and one half of the cell is filled with magnetic fluid because of capillary forces. Then the magnetic field is switched on, and a small amount of the non-magnetic fluid is added to the other side of the cell using a small tube and a syringe with a microscrew until the solvent comes into contact with the magnetic fluid.

The homogeneous magnetic field with strength $H \in (0–300)$ Oe is created in the central part of the coil where the Hele-Shaw cell is placed. The coil with diameter 34 mm and height 16 mm consists of 38 turns of 0.7 mm wire.

The theoretical analysis (Cebers 1997; Igonin & Cebers 2003) and numerical calculations described in Part 2 show that the smearing of the diffusion front between the two miscible fluids plays an important role in the development of the magnetic micro-convection.

The experimental data shown in figure 7 clearly confirm the existence of the critical value of the field strength below which the fingering due to the magnetic micro-convection is not observed. If we estimate the critical field strength according to the data shown in figure 7 to be 3.4 G, the magnetic Rayleigh number for the fluid with the given physical properties is $Ra_m = 1150$, a value much larger than the critical value corresponding to $t_0 = 0$ and shown in figure 3. Figure 3 shows that such large values of the critical magnetic Rayleigh number correspond to large values of the smearing

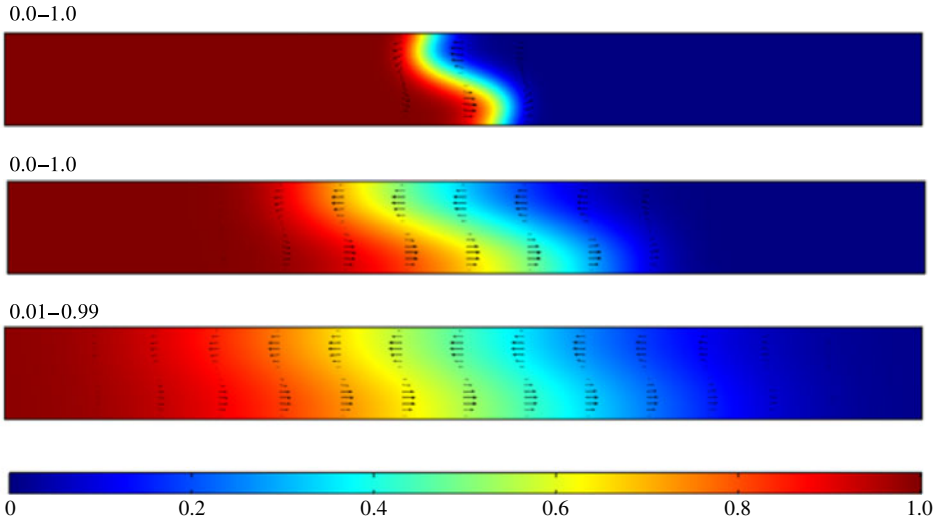

FIGURE 8. Concentration field at $t = 0.1$, 1, 5 and $Ra = 400$.

parameter, which should not be expected if the particle diffusion were dominant. Large smearing may be explained by the effect of the gravitational force. Although the densities of the magnetic and carrier liquids are similar, nevertheless a simple estimate shows that the gravitational Rayleigh number $Ra = \Delta\varrho g h^3/8D\eta$ at a density difference of 0.077 g cm^{-3} is quite large and exceeds 3.5×10^4. As a result, after the liquids make contact counterflows arise in the lower and upper parts of the Hele-Shaw cell. Their role in the smearing of the interface may be illustrated by the Stokes model with the concentration c dependent gravity force and the diffusion equation. Scaling time by $h^2/4D$, length by $h/2$ and the velocity by $\Delta\rho g h^2/4\eta$ (h is the thickness of the Hele-Shaw cell), the dimensionless set of partial differential equations (PDEs) reads

$$-\boldsymbol{\nabla} p + \nabla^2 \boldsymbol{v} - c\boldsymbol{e}_y = 0, \tag{3.1}$$

$$\frac{\partial c}{\partial t} + Ra(\boldsymbol{v} \cdot \boldsymbol{\nabla})c = \nabla^2 c. \tag{3.2}$$

The evolution of the concentration field and the liquid flow are calculated by using the Comsol software with the initial concentration distribution given by $c_0(x, t_0)$ at $t_0 = 0.025$:

$$c_0(x, 0) = \frac{1}{2}\left(1 - \frac{2}{\sqrt{\pi}} \int_0^{x/(2\sqrt{t_0})} \exp(-y^2)\, \mathrm{d}y\right). \tag{3.3}$$

The results for $Ra = 400$ (the results for other values of the Rayleigh number are qualitatively the same) in the cell $x \in [-10 : 10]$ and $y \in [-1 : 1]$ are shown in figures 8 and 9. The calculated concentration distribution in the middle of the cell ($y = 0$) at different time moments and the evolution of the horizontal component of the velocity in the middle cross-section of the cell ($x = 0$) are shown in figures 10 and 11, respectively. We see that the flow due to gravity smears out the concentration distribution and, after some transition time, the concentration distribution with a much wider transition layer is established, as may be seen in figure 8. The time dependence of the maximal value of the velocity of the arising flow for different values of the

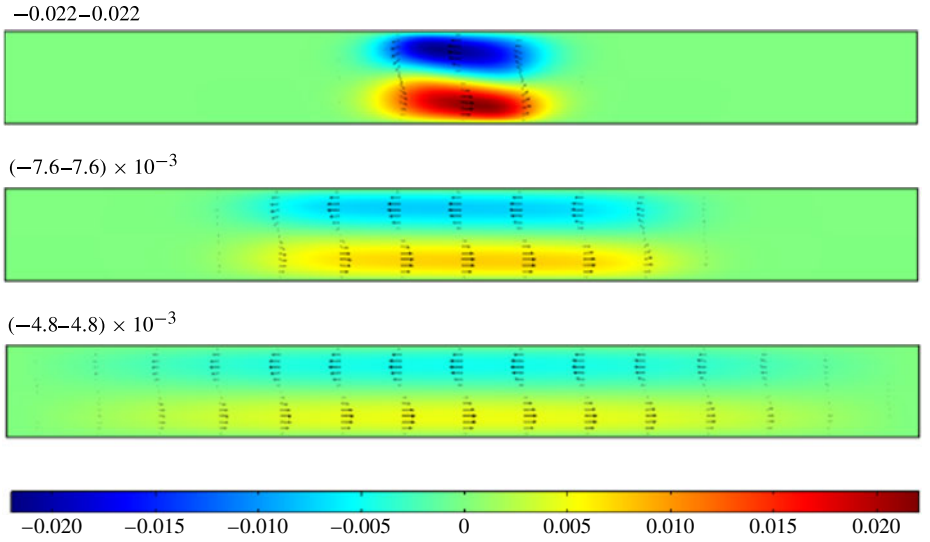

FIGURE 9. Evolution of the horizontal velocity field at $t = 0.1, 1, 5$ and $Ra = 400$.

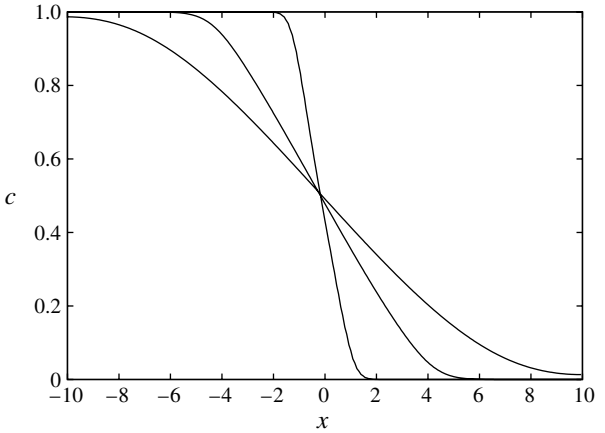

FIGURE 10. Smearing of the concentration distribution due to the flow caused by gravity at $t = 0.1, 1, 5$ and $Ra = 400$.

Rayleigh number is shown in figure 12. Thus, we see that gravity causes considerable smearing of the interface before the fingering due to the magnetic micro-convection starts. This result explains the rather large values of the magnetic Rayleigh number necessary for its initiation.

Estimating the characteristic velocity of the flow caused by gravity according the data in figure 12 by $v = 10^{-2}\Delta\varrho g h^2/4\eta$ in dimensional units that give the characteristic velocity of flow as 31 μm s^{-1}, we see that it is close to the values determined from the contrast variation of the interface observed in the experiment and shown in figure 13. The characteristic times of the decay of the flow caused by gravity $0.1h^2/4D \simeq 70$ s are also in agreement.

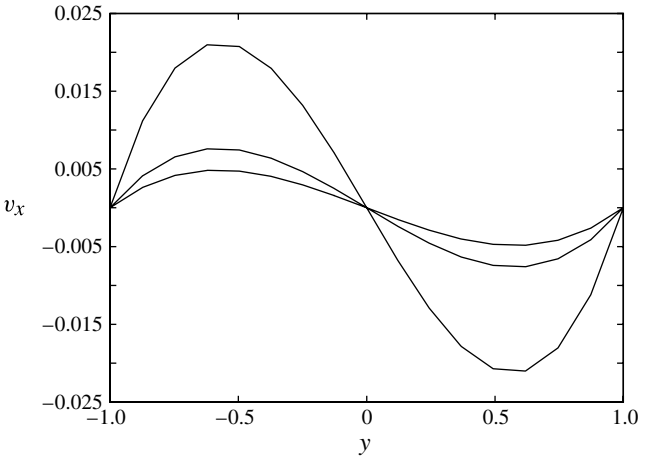

FIGURE 11. Horizontal component of velocity in the middle cross-section of the cell for different dimensionless time moments $t = 0.1, 1, 5$ and $Ra = 400$.

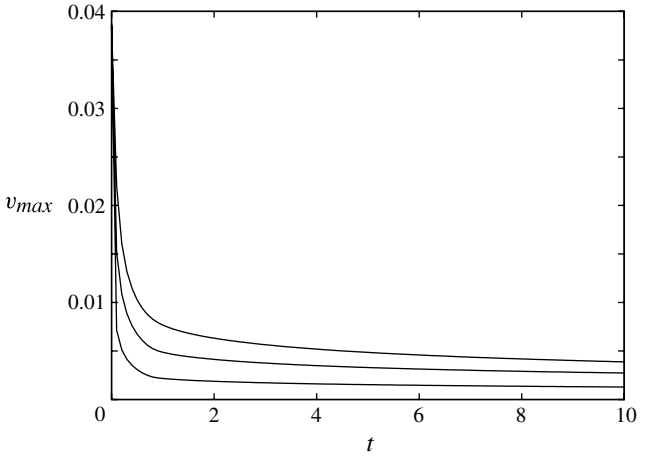

FIGURE 12. Time dependence of the maximal horizontal velocity with $Ra = 400, 1000, 5000$.

The experimental results of the development of magnetic micro-convection for several values of the magnetic field strength are shown in figure 14. The patterns are similar to those observed in numerical experiments for moderate values of the magnetic Rayleigh number and shown in figure 4. The grainy structure of the interface, which may be seen in figure 14 for larger values of the field (18 and 27 G), is caused by the normal field instability (Rosensweig 1985) of the layer of magnetic fluid formed by the gravitational convection.

The estimates that confirm that the grainy structure, which may be seen in figure 14 for larger values of the field is caused by the normal field instability are given in appendix B. The results for the critical field strength and the structure period given the physical parameters of liquids described above are in good agreement with the

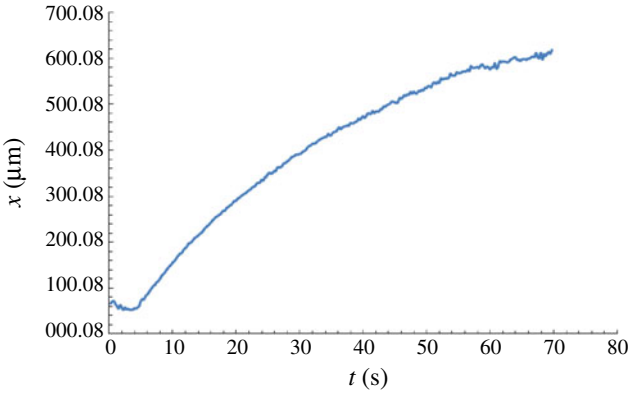

FIGURE 13. (Colour online) Experimental data of the propagation of the interface at a magnetic field value of 2.25 G.

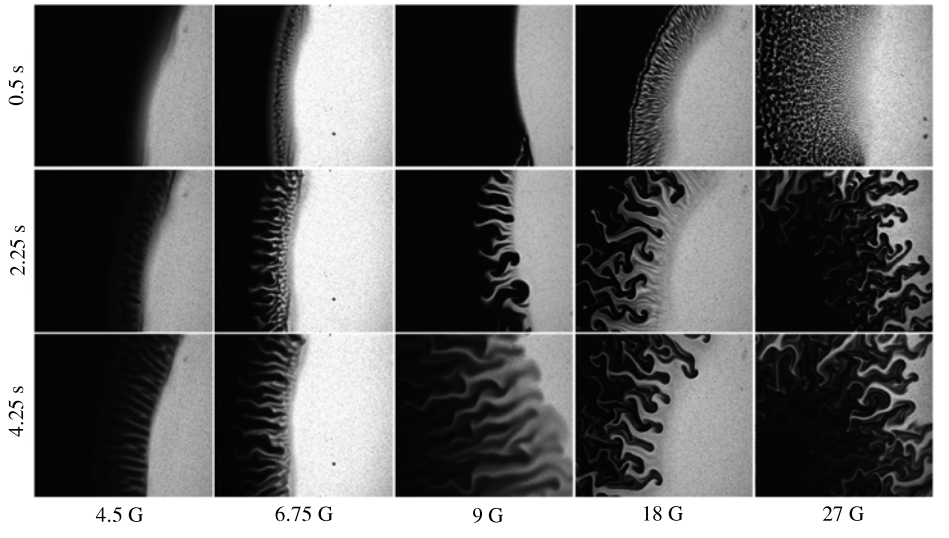

FIGURE 14. Fingering instability development in dependence on the magnetic field strength.

experiment (figure 14). In order to check that the stratification resulting from the flow due to gravity and subsequent normal field instability indeed cause the grainy structure, a glycerol–water mixture with density matched to the density of the magnetic fluid was prepared. The fingering at the interface of magnetic and non-magnetic fluids with matched densities for field of 27 G is shown in figure 15. We clearly see that the grainy structure is absent now. This result and the estimates given in appendix B confirm that the grainy structure is caused by the normal field instability on the interface between two miscible fluids. It should be mentioned here that matching the density of the magnetic fluid is a subtle issue since it is impossible to use salt solution which causes the coagulation of the electrostatically stabilized magnetic fluid. Using the glycerol–water solution creates another problem: the viscosity of the glycerol–water solution is higher than the viscosity of the ferrofluid. Nevertheless,

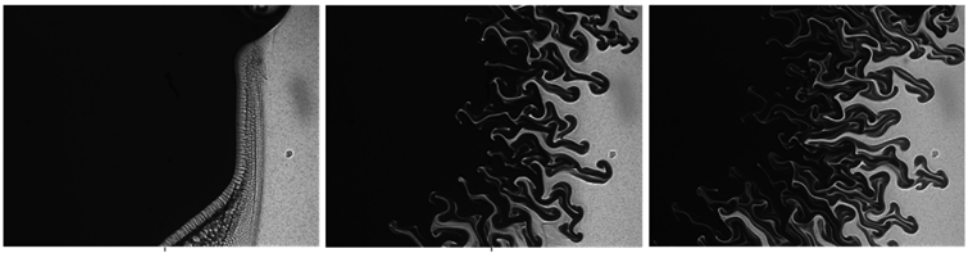

FIGURE 15. Fingering at the interface between the fluids with matched densities, with $B = 27$ G.

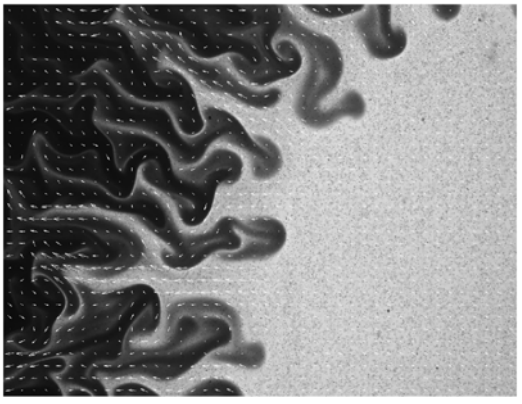

FIGURE 16. Vector field at time 8.5 s and $B = 18$ G.

we believe that the reason of the grainy structure formation now is confirmed both theoretically and experimentally. Some small-scale stripe-like structure which may be seen in figure 15 is caused by the fingering phenomenon on the borders of the Hele-Shaw cell wetted by the ferrofluid.

Thus, the full model of the magnetic micro-convection is much more complicated as considered here and should incorporate three-dimensional equations for the magnetic field, concentration and flow.

Quantitative information about the velocity field of the micro-convection is obtained by PIV measurements. The main problem of using PIV algorithms for magnetic micro-convection is that it is impossible to determine the fluid flow in the darker regions because of poor image contrast. Therefore, special image-processing algorithms had been developed to improve the contrast (Ergin *et al.* 2010). This algorithm includes image preprocessing for local image normalization and a Gaussian filter in order to reduce noise. The vector field after preprocessing is obtained by an adaptive correlation algorithm with 2 refined steps, 2 passes per step, 32-pixel-wide interrogation windows with 50 % overlap. The velocity field of the fingering pattern obtained at $H = 180$ Oe and $t = 8.5$ s is shown in figure 16. Vortices formation similar to that observed in numerical experiments (figure 5) is visible.

The values of the fingering velocity for one value of the field strength are shown in figure 17. Maximal value of the fingering velocity may be compared

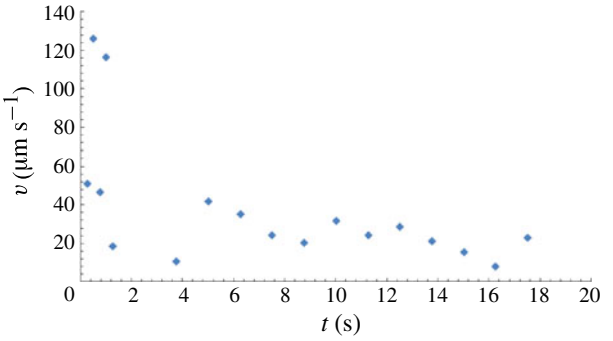

FIGURE 17. (Colour online) Finger velocity in dependence on time at a magnetic field value of 6.75 G.

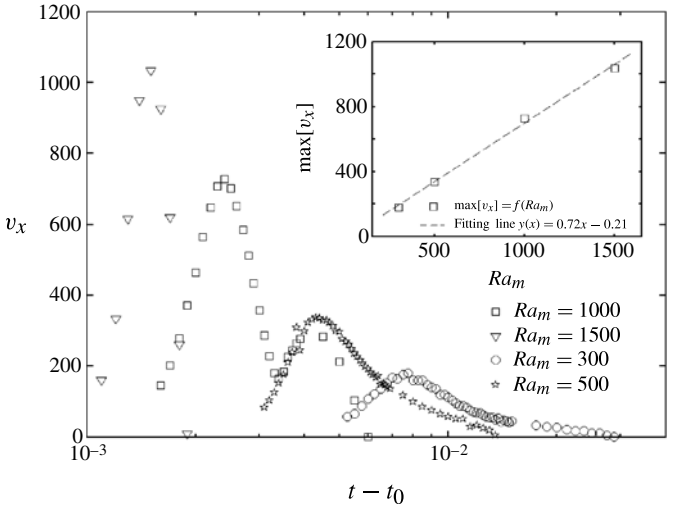

FIGURE 18. Finger velocity in dependence on time at different values of the magnetic Rayleigh number $Ra_m = 300$, 500, 1000 and 1500, with $t_0 = 0.05$.

with data obtained from numerical calculations. Finger velocities in dependence on time obtained from the numerical simulations at several values of the magnetic Rayleigh number are shown in figure 18. Its maximal value may be fitted by $\max(v_x) = 0.72Ra_m$. As a result, the dimensional velocity of fingering for the physical parameters of the ferrofluid given above at field strength 6.75 G is equal to 142 μm s^{-1}: a value very close to that obtained in the experiments (figure 17).

By using the obtained velocity field, vorticity values are calculated with the Dantec dynamics software, which uses the neighbouring window velocity value difference to find the vorticity for each window. Afterwards we export the vorticity field values and post process them using MATLAB to extract the necessary information, e.g. the maximum absolute vorticity time dependence, shown in figure 19. Thus, the developed algorithm allows us to obtain the evolution of the vorticity field during the development of the magnetic micro-convection and its decay due to the diffusion of the magnetic nanoparticles. It may be characterized by a rapid increase of the vorticity

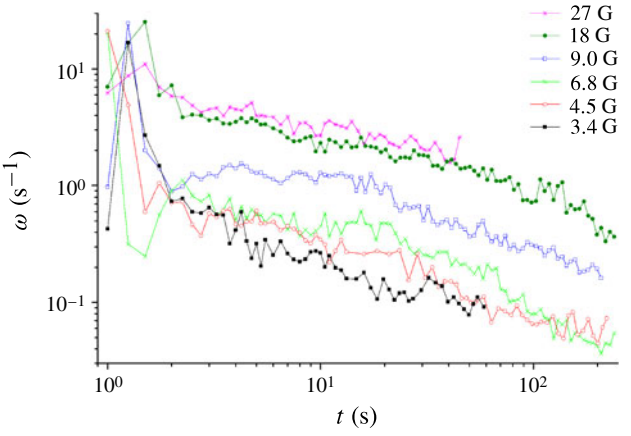

FIGURE 19. Vorticity dependence on time for different magnetic field values.

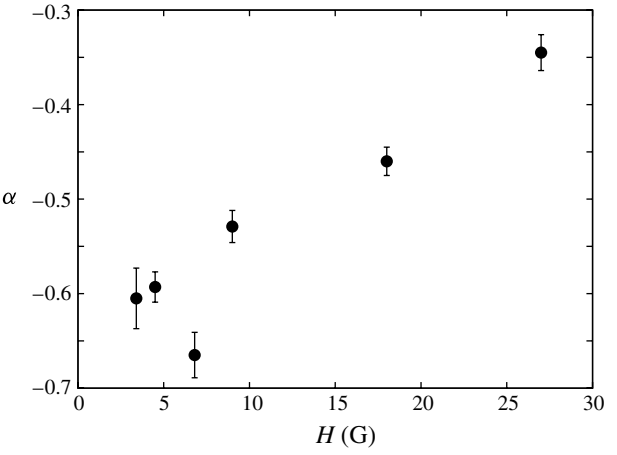

FIGURE 20. The exponent of the power law α for different magnetic field values.

followed by its slow decay. Again a qualitative similarity between the numerical data figure 6 and experimental data figure 19 is observed. Experimental data for the vorticity decay may be fitted by the power law $\omega_{max} \sim t^{\alpha}$. The values of the exponent α obtained are shown in figure 20. This figure illustrates the increase of the exponent with the field strength, which corresponds to the slower decay of the fingering at larger fields. This trend correlates with the increase of the exponent obtained in the numerical simulations at several values of the magnetic field strength shown in figure 6.

4. Conclusions

The proposed model of the magnetic micro-convection qualitatively describes the experimental data on the development and decay of the magnetic micro-convection as shown by the results of numerical simulations. The characteristic feature of the magnetic-field-driven micro-convection is an initial fast development of the fingering

with a subsequent decay of the flow due to the diffusion of the nanoparticles. As a result considerable enhancement of the mixing is achieved, which may be interesting for some applications of the magnetic nanoparticles in microfluidics. The smearing of the diffusion front caused by the action of gravity force because of the small density difference between the magnetic colloid and its solvent plays an important role in the threshold value of the magnetic field strength for the development of the magnetic micro-convection. Stratification caused by gravitational convection is the reason for the development of the normal field instability. The theoretical analysis of the normal field instability on the interface between two miscible fluids shows good agreement with the experimental observations.

Acknowledgement

This work was supported by the ESF project 2009/0223/1DP/1.1.1.2.0/APIA/VIAA/008.

Appendix A. Numerical algorithm

In order to apply spectral methods and the fast Fourier transform (FFT) we represent the concentration by a sum of two parts:

$$c(x, y, t) = c_D(x, t) + c'(x, y, t), \tag{A 1}$$

where $c_D(x, t)$ is given by the solution of the one-dimensional convection–diffusion equation as $c_D(x, t) = 0.5(1 - \mathrm{erf}(x/\sqrt{4t}))$ and corresponds to a step-like concentration at $t = 0$. The concentration perturbation c' is a periodic function in the x, y directions ($c'(x, y) = c'(x + L_x, y + L_y)$). As a result, the numerical solution should be found for the periodic function $c'(x, y)$.

Similarly, the magnetostatic potential is split into two contributions

$$\psi_m(x, y, t) = \psi_m^D(x, t) + \psi_m'(x, y, t), \tag{A 2}$$

here

$$\psi_m^D(x, t) = \int_{-\infty}^{+\infty} c_D(x - \zeta, t) \ln(1 + \zeta^{-2})\, \mathrm{d}\zeta, \tag{A 3a}$$

$$\psi_m'(\boldsymbol{r}) = \int_S c'(\boldsymbol{r}', t)\mathrm{K}(\boldsymbol{r} - \boldsymbol{r}', 1)\, \mathrm{d}S'. \tag{A 3b}$$

Integration in (A 3*a*) is carried out through all of the infinite region occupied by the magnetic fluid. The fast decay of the field strength $\partial\psi_m^D/\partial x$ with the distance from the diffusion front justify the use of periodic boundary conditions. Integration in (A 3*b*) is carried out along the cell with dimensions L_x and L_y.

The Fourier component of $\partial\psi_m^D/\partial x$ is obtained by using the convolution theorem according to the relation:

$$\frac{\partial\hat{\psi}_m^D}{\partial x}(k_n) = 2\pi\frac{\partial\hat{c}_D}{\partial x}(k_n)\frac{1 - \mathrm{e}^{-|k_n|}}{|k_n|}, \tag{A 4}$$

where the Fourier coefficients $\partial\hat{c}_D/\partial x$ are calculated by a one-dimensional FFT (the domain size is increased in the x direction from L_x to $4L_x$ to eliminate the Gibbs phenomenon).

The perturbation of the concentration at the initial time is introduced by a small displacement $\varsigma(y)$ of the isoline $c = 0.5$ at $x = x_0$ (for all numerical

calculations $x_0 = L_x/2$) according to the relation

$$c(x, y, t_0) = \frac{1}{2}\left(1 - \mathrm{erf}\left(\frac{x - x_0 + \varsigma(y)}{\sqrt{4t_0}}\right)\right), \tag{A 5}$$

where t_0 is the parameter that characterizes the smearing.

The small perturbation ς is defined by the Fourier series $\varsigma(y) = \sum_{n=1}^{N}[a_n \cos(qyn) + b_n \sin(qyn)]$ $(q = 2\pi/L_y)$.

For the test of the results of linear analysis

$$c(x, y, t_0) = \frac{1}{2}\left(1 - \mathrm{erf}\left(\frac{x - x_0}{\sqrt{4t_0}}\right)\right) + \varsigma(x, y), \tag{A 6}$$

where the amplitudes of perturbation modes a_n, b_n are defined by eigenfunctions found theoretically and read $\{a_n, b_n\} = \{\varepsilon_a, \varepsilon_b\}\mathrm{e}^{-qn\sqrt{1+\lambda/(n^2q^2)}|x-x_0|}$ (λ is given by the dispersion relation (2.8) for fixed value of magnetic Rayleigh number Ra_m).

Equations (2.6) and (2.7) are solved numerically by the spectral method in the vorticity stream function formulation (Tan & Homsy 1988; Zimmerman & Homsy 1992). The stream function ψ is defined as $u_x = \partial\psi/\partial y$ and $u_y = -\partial\psi/\partial x$, and the vorticity ω is

$$\omega = -\nabla^2\psi. \tag{A 7}$$

Taking into account (A 1) the convection–diffusion equation (2.7) can be written as follows

$$\frac{\partial c'}{\partial t} = \frac{\partial^2 c'}{\partial x^2} + \frac{\partial^2 c'}{\partial y^2} - \frac{\partial\psi}{\partial y}\left(\frac{\partial c_D}{\partial x} + \frac{\partial c'}{\partial x}\right) + \frac{\partial\psi}{\partial x}\frac{\partial c'}{\partial y}. \tag{A 8}$$

Equation (2.6) gives the vorticity equation

$$\omega = -2Ra_m\left(\frac{\partial\psi_m}{\partial y}\left[\frac{\partial c_D}{\partial x} + \frac{\partial c'}{\partial x}\right] - \frac{\partial\psi_m}{\partial x}\frac{\partial c}{\partial y}\right). \tag{A 9}$$

In order to solve numerically (A 8) and (A 9) the Fourier spectral method is used. The concentration perturbation c', stream function ψ and vorticity ω are presented by the Fourier series

$$c'(x, y, t) = \sum_{n=0}^{N-1}\sum_{m=0}^{M-1}\hat{c}_{nm}(t)\mathrm{e}^{\mathrm{i}(k_n x + q_m y)}, \tag{A 10a}$$

$$\psi(x, y, t) = \sum_{n=0}^{N-1}\sum_{m=0}^{M-1}\hat{\psi}_{nm}(t)\mathrm{e}^{\mathrm{i}(k_n x + q_m y)}, \tag{A 10b}$$

$$\omega(x, y, t) = \sum_{n=0}^{N-1}\sum_{m=0}^{M-1}\hat{\omega}_{nm}(t)\mathrm{e}^{\mathrm{i}(k_n x + q_m y)} \tag{A 10c}$$

where $k_n = 2\pi n/L_x$, $q_m = 2\pi m/L_y$ are wavenumbers $(n, m = 0, 1, 2\ldots)$. Functions $\hat{c}_{nm}$, $\hat{\psi}_{nm}$ and $\hat{\omega}_{nm}$ are calculated by using FFT in collocation points $x_n = (L_x/N)n$ and $y_m = (L_y/N)m$ $(n = 0, 1, 2\ldots N-1,\ m = 0, 1, 2\ldots M-1)$. The total number of collocation points N, M is proportional to 2^p, $p = 1, 2, 3\ldots$ and depend on the concrete case.

The nonlinear terms in (A 8) and (A 9) are given by applying a FFT:

$$J(x,y,t)=\frac{\partial\psi}{\partial y}\left(\frac{\partial c_D}{\partial x}+\frac{\partial c'}{\partial x}\right)-\frac{\partial\psi}{\partial x}\frac{\partial c'}{\partial y}=\sum_{n=0}^{N-1}\sum_{m=0}^{M-1}\hat{\mathrm{J}}_{nm}(t)\mathrm{e}^{\mathrm{i}(k_nx+q_my)}, \tag{A 11a}$$

$$Q(x,y,t)=\frac{\partial\psi_m}{\partial y}\left(\frac{\partial c_D}{\partial x}+\frac{\partial c'}{\partial x}\right)-\frac{\partial\psi_m}{\partial x}\frac{\partial c'}{\partial y}=\sum_{n=0}^{N-1}\sum_{m=0}^{M-1}\hat{Q}_{nm}(t)\mathrm{e}^{\mathrm{i}(k_nx+q_my)}. \tag{A 11b}$$

As a result, the equations for the amplitudes of the Fourier modes read

$$\hat{\omega}_{nm}=(k_n^2+q_m^2)\hat{\psi}_{nm}, \tag{A 12}$$

$$\hat{\omega}_{nm}=-2Ra_m\hat{Q}_{nm}, \tag{A 13}$$

$$\frac{\partial\hat{c}_{nm}}{\partial t}=-(k_n^2+q_m^2)\hat{c}_{nm}-\hat{\mathrm{J}}_{nm}. \tag{A 14}$$

The values of the stream function $\psi(t_j)$ for given values of the concentration $c(t_j)$ are found from (A 12) and (A 13). Since ψ'_m is periodic in both the x and y directions, $\hat{\psi}'_m(\boldsymbol{k})$ is obtained as follows:

$$\hat{\psi}'_m(\boldsymbol{k})=2\pi\hat{c}_{nm}(\boldsymbol{k})\hat{T}_{nm}(\boldsymbol{k}), \tag{A 15}$$

where $\boldsymbol{k}=(k_n,q_m)$ is the two-dimensional wave vector and $|\boldsymbol{k}|=\sqrt{k_n^2+q_m^2}$. The Fourier coefficients $\hat{c}_{nm}$ are calculated using a two-dimensional FFT algorithm and $\hat{T}_{nm}(\boldsymbol{k})=(1-\mathrm{e}^{-|\boldsymbol{k}|})/|\boldsymbol{k}|$ is the Fourier transform of $K(\boldsymbol{r},1)$. All derivatives of ψ'_m are calculated spectrally from the obtained values of $\hat{\psi}'_m(\boldsymbol{k})$.

The linear equation (A 14) is solved for the known stream function by applying the linear propagator method, which factors out the leading-order linear term prior to the discretization. Introducing $\hat{\chi}_{nm}=\mathrm{e}^{(k_n^2+q_m^2)t}\hat{c}_{nm}$ the equation $\partial\hat{\chi}_{nm}/\partial t=-\mathrm{e}^{(k_n^2+k_m^2)t}\hat{\mathrm{J}}_{nm}$ is discretized by using the three-step Adams–Bashforth method (Samarskij & Gulin 1989). The result reads

$$\hat{c}_{nm}^{(j+1)*}=\hat{c}_{nm}^{j}\gamma-\frac{\Delta t}{12}(23\hat{\mathrm{J}}_{nm}^{j}\gamma-16\hat{\mathrm{J}}_{nm}^{(j-1)}\gamma^2+5\hat{\mathrm{J}}_{nm}^{(j-2)}\gamma^3), \tag{A 16}$$

$$\gamma=\mathrm{e}^{-(k_n^2+k_m^2)\Delta t}. \tag{A 17}$$

Further, corrected values of $\psi_{nm}^{(j+1)*}$ and $\hat{\mathrm{J}}_{nm}^{(j+1)*}$ are found from (A 12), (A 13) and (A 11*a*), respectively. As a result, the Fourier components of the concentration are obtained for the next time step

$$\hat{c}_{nm}^{(j+1)}=\hat{c}_{nm}^{j}-\frac{\Delta t}{2}(\hat{\mathrm{J}}_{nm}^{(j+1)*}+\hat{\mathrm{J}}_{nm}^{j})-\frac{\Delta t}{2}(k_n^2+k_m^2)(\hat{c}_{nm}^{(j+1)*}+\hat{c}_{nm}^{j}). \tag{A 18}$$

The concentration field is obtained by applying the inverse FFT to $\hat{c}_{nm}^{(j+1)}$ and adding $c_D(t)$. Since the numerical scheme used is not fully implicit in time, the solution may show numerical instability.

Appendix B. Normal field instability at the interface of miscible magnetic and non-magnetic fluids

Normal field instability of the free horizontal surface of a magnetic liquid is well understood. However, this instability has not been considered yet in the case of the interface between two miscible fluids. In this appendix it is shown that in the case

when $t_0 \to 0$ it is possible to obtain analytically the dispersion equation for the growth increment of the instability.

The Stokes equation in the case of miscible liquids and the diffusion equation for the particle concentration read

$$-\nabla p + \eta\nabla^2\boldsymbol{v} + \chi_0 c\nabla\left(\frac{H^2}{2}\right) - \Delta\rho c g\boldsymbol{e}_z = 0, \quad \nabla\cdot\boldsymbol{v} = 0, \tag{B 1}$$

$$\frac{\partial c}{\partial t} + \boldsymbol{v}\cdot\nabla c = D\nabla^2 c, \tag{B 2}$$

where the z-axis is along the vertical direction, c is the concentration of magnetic particles normalized to 1 by the concentration far from the interface, and $\Delta\rho$ is the density difference of the magnetic and non-magnetic liquids.

At equilibrium when the magnetic field is parallel to the gradient of the concentration c_0 it reads

$$\boldsymbol{H} = \boldsymbol{H}_0 = (0, 0, H_\infty/(1 + 4\pi\chi_0 c_0)). \tag{B 3}$$

Here H_∞ is the magnetic field strength far from the interface in the non-magnetic liquid and χ_0 is the magnetic susceptibility.

The equation for the magnetic field in the case of small perturbations around $c = c_0(z)$ reads (with $c = c_0 + c'$, $\boldsymbol{H} = \boldsymbol{H}_0 + \boldsymbol{H}'$ and $\boldsymbol{H}' = \nabla\psi'$)

$$\frac{\partial}{\partial x}((1 + 4\pi\chi_0 c_0)H'_x) + \frac{\partial}{\partial z}(4\pi\chi_0 c' H_{0z}) + \frac{\partial}{\partial z}((1 + 4\pi\chi_0 c_0)H'_z) = 0. \tag{B 4}$$

In the limit when c_0 is step-like, it follows from (B 4) that

$$H = (1 + 4\pi\chi_0 c_0)H'_z + \frac{4\pi\chi_0 c' H_\infty}{1 + 4\pi\chi_0 c_0} \tag{B 5}$$

is continuous on the interface where $c_0(0^+) = 0$ and $c_0(0^-) = 1$.

The equations for the velocity and concentration perturbations read

$$-\nabla p' + \eta\nabla^2\boldsymbol{v} + \chi_0 c_0\nabla(\boldsymbol{H}_0\cdot\boldsymbol{H}') - \Delta\rho c' g\boldsymbol{e}_z = 0 \tag{B 6}$$

and

$$\frac{\partial c'}{\partial t} + v_z\frac{\mathrm{d}c_0}{\mathrm{d}z} = D\nabla^2 c'. \tag{B 7}$$

Looking for perturbations periodic in the horizontal direction

$$(\boldsymbol{v}', c', \psi') = (\boldsymbol{v}(z), c(z), \psi(z))\exp(\mathrm{i}kx), \tag{B 8}$$

we have

$$\frac{\partial c}{\partial t} + v_z\frac{\mathrm{d}c_0}{\mathrm{d}z} = D\left(\frac{\mathrm{d}^2 c}{\mathrm{d}z^2} - k^2 c\right), \tag{B 9}$$

$$\eta\left(\frac{\mathrm{d}^2}{\mathrm{d}z^2} - k^2\right)^2 v_z = -\frac{\chi_0 k^2 H_\infty}{1 + 4\pi\chi_0 c_0}\frac{\mathrm{d}c_0}{\mathrm{d}z}H - \Delta\rho c g k^2, \tag{B 10}$$

$$\frac{\mathrm{d}}{\mathrm{d}z}\left((1 + 4\pi\chi_0 c_0)\frac{\mathrm{d}\psi}{\mathrm{d}z}\right) - (1 + 4\pi\chi_0 c_0)k^2\psi + \frac{\mathrm{d}}{\mathrm{d}z}(4\pi\chi_0 c H_{0z}) = 0. \tag{B 11}$$

For step-like $c_0(z)$ the boundary conditions are obtained by integration $\int_{-\delta}^{\delta}\mathrm{d}z(\cdots)$ of (B 9)–(B 11) across the diffusion layer and taking the limit $\delta \to 0$. They

read ($\mu_\infty = 1 + 4\pi\chi_0$)

$$\left.\begin{aligned}
&c(0^+) = c(0^-),\\
&D\frac{\mathrm{d}c}{\mathrm{d}z}(0^+) - D\frac{\mathrm{d}c}{\mathrm{d}z}(0^-) = -v_z(0),\\
&v_z(0^+) = v_z(0^-),\\
&\frac{\mathrm{d}v_z}{\mathrm{d}z}(0^+) = \frac{\mathrm{d}v_z}{\mathrm{d}z}(0^-),\\
&\frac{\mathrm{d}^2v_z}{\mathrm{d}z^2}(0^+) = \frac{\mathrm{d}^2v_z}{\mathrm{d}z^2}(0^-),\\
&\frac{\mathrm{d}^3v_z}{\mathrm{d}z^3}(0^+) - \frac{\mathrm{d}^3v_z}{\mathrm{d}z^3}(0^-) = \frac{(\mu_\infty - 1)k^2H_\infty}{4\pi\eta\mu_\infty}H(0),\\
&\psi(0^+) = \psi(0^-),\\
&\frac{\mathrm{d}\psi_z}{\mathrm{d}z}(0^+) + (\mu_\infty - 1)c(0)H_\infty = \mu_\infty\frac{\mathrm{d}\psi_z}{\mathrm{d}z}(0^-) + \frac{(\mu_\infty - 1)c(0)H_\infty}{\mu_\infty}.
\end{aligned}\right\} \tag{B 12}$$

Equations (B 9)–(B 11) at boundary conditions (B 12) are analysed in the quasi-stationary case when $\boldsymbol{v}, c, \psi \sim \exp(\lambda t)$. The solutions of (B 9)–(B 11) that satisfy the condition $\boldsymbol{v}, c, \psi \to 0$ at $|z| \to \infty$ and the boundary conditions for the magnetostatic potential and concentration read

$$\left.\begin{aligned}
&c = E\exp(-\sqrt{\lambda/D + k^2}z) \quad (z > 0),\\
&c = E\exp(\sqrt{\lambda/D + k^2}z) \quad (z < 0),\\
&\psi = -\frac{(\mu_\infty - 1)H_\infty E}{\lambda/D\mu_\infty(\mu_\infty + 1)}(\sqrt{\lambda/D + k^2}(\mu_\infty^2 + 1) + (\mu_\infty - 1)k)\exp(-kz)\\
&\quad + \frac{(\mu_\infty - 1)H_\infty}{\lambda/D}\sqrt{\lambda/D + k^2}\exp(-\sqrt{\lambda/D + k^2}z)E \quad (z > 0),\\
&\psi = \frac{(\mu_\infty - 1)H_\infty E}{\lambda/D\mu_\infty(\mu_\infty + 1)}(\sqrt{\lambda/D + k^2}(\mu_\infty^2 + 1) - (\mu_\infty - 1)k)\exp(kz)\\
&\quad - \frac{(\mu_\infty - 1)H_\infty}{\lambda/D\mu_\infty^2}\sqrt{\lambda/D + k^2}\exp(\sqrt{\lambda/D + k^2}z)E \quad (z > 0),\\
&v_z = C\exp(-kz) + Dz\exp(-kz) - \frac{\Delta\rho g k^2 E}{\eta\,(\lambda/D)^2}\exp(-\sqrt{\lambda/D + k^2}z) \quad (z > 0),\\
&v_z = A\exp(kz) + Bz\exp(kz) - \frac{\Delta\rho g k^2 E}{\eta\,(\lambda/D)^2}\exp(\sqrt{\lambda/D + k^2}z) \quad (z < 0).
\end{aligned}\right\} \tag{B 13}$$

The remaining five boundary conditions give the set of five equations for the unknown set of constants A, B, C, D, E. Its solubility condition gives the dispersion equation for the growth increment of small perturbations

$$\begin{aligned}
&\frac{4\sqrt{\lambda/D + k^2}}{k} - \frac{(\mu_\infty - 1)^2(\mu_\infty^2 + 1)H_\infty^2}{8\pi\eta D\mu_\infty^2(\mu_\infty + 1)}\frac{\sqrt{\lambda/D + k^2} - k}{\lambda/Dk}\\
&\quad = \frac{\Delta\rho g}{D\eta}\frac{\sqrt{\lambda/D + k^2}(2k^2 - \lambda/D) - 2k^3}{k\,(\lambda/D)^2}.
\end{aligned} \tag{B 14}$$

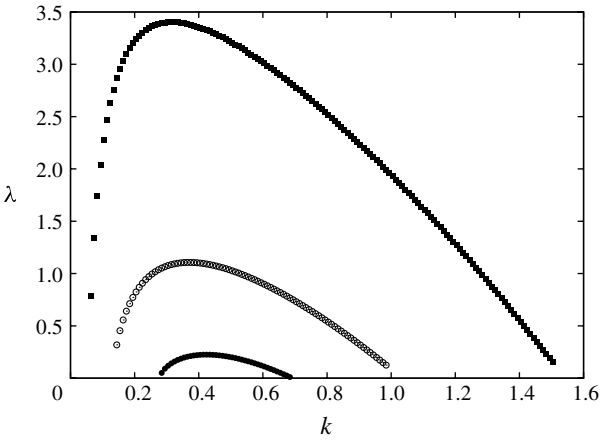

FIGURE 21. Growth increments of the normal field instability at the interface of two miscible fluids in dependence on the wavenumber at different values of the magnetic Rayleigh number. Here $Ra_m^c = 6$ (black circles), $Ra_m^c = 10$ (open circles) and $Ra_m^c = 20$ (squares).

There are two characteristic lengths in the problem: the magnetic length,

$$l_H^{-2} = \frac{(\mu_\infty - 1)^2(\mu_\infty^2 + 1)H_\infty^2}{8\pi\eta D\mu_\infty^2(\mu_\infty + 1)}, \tag{B 15}$$

and the gravitational length,

$$l_G^{-3} = \frac{\Delta\rho g}{D\eta}. \tag{B 16}$$

On the scales l_H and l_G, the magnetic and gravitational Rayleigh numbers, respectively, are equal to one. Choosing as the characteristic scale of the wavenumber $(\Delta\rho g/(D\eta))^{1/3}$, the dispersion equation in dimensionless form reads ($\tilde{\lambda} = \lambda l_G^2/D$, where $Ra_m = (l_G/l_H)^2$ is the magnetic Rayleigh number defined by the characteristic gravitational length, tildes are further omitted)

$$\frac{4\sqrt{\lambda + k^2}}{k} - Ra_m\frac{\sqrt{\lambda + k^2} - k}{k\lambda} = \frac{\sqrt{\lambda + k^2}(2k^2 - \lambda) - 2k^3}{k^2\lambda^2}. \tag{B 17}$$

In the limit $\lambda \to 0$, equation (B 17) gives

$$Ra_m = \frac{3}{2k} + 8k^2. \tag{B 18}$$

This gives for the critical magnetic Rayleigh number Ra_m^c and wavenumber k_*

$$Ra_m^c = 24k_*^2, \quad k_* = (3/32)^{1/3}. \tag{B 19}$$

The dependence of the growth increment on the dimensionless wavenumber for several values of the magnetic Rayleigh number is shown in figure 21.

The obtained results give values for the characteristic period of the pattern arising at the normal field instability and the critical magnetic field strength, which have the same order of magnitude as observed in the experiment. The critical value of the magnetic Rayleigh number for the critical field in the case of the physical properties

of the magnetic liquid and the density difference of the liquids for the critical magnetic field strength and the period of the pattern give the values $H_c = 2.47$ G and $2\pi/k_* = 27$ μm, respectively. These values are close to those observed in the experiment. As one can see, the formation of the grainy structure on the interface already appears at field strength of 6.75 G: a value quite close to our estimates. The period of the structure 20 μm estimated by counting the number of black dots 20 which are seen in figure 14 on the length scale 4×10^{-2} cm also is close to our estimate.

It should be remarked that scales of this phenomenon are completely different from the classical normal field instability, whose scale is determined by the capillary length and is of the order of centimetres.

REFERENCES

CABRAL, B. & LEEDOM, L. 1993 Imaging vector fields using line integral convolution. *Proc. ACM* **93**, 263–270.

CEBERS, A. 1981 Dynamics of magnetostatic instabilities. *Magnetohydrodynamics* **17**, 113–121.

CEBERS, A. 1997 Stability of diffusion fronts of magnetic particles in porous media under the action of external magnetic field. *Magnetohydrodynamics* **33**, 48–55.

CEBERS, A. & MAIOROV, M. M. 1980 Magnetostatic instabilities in plane layers of magnetizable fluids. *Magnetohydrodynamics* **16**, 21–27.

CHEN, C.-Y. 2003 Numerical simulations of fingering instabilities in miscible magnetic fluids in a Hele-Shaw cell and the effect of Korteweg stress. *Phys. Fluids* **15**, 1086–1089.

CHEN, C.-Y. & WEN, C.-Y. 2002 Numerical simulations of miscible magnetic flows in a Hele-Shaw cell. Radial flows. *J. Magnetism Magnetic Mater.* **252**, 296–298.

DEREC, C., BOLTENHAGEN, P., NEVEU, S. & BACRI, J.-C. 2008 Magnetic instability between miscible fluids in a Hele-Shaw cell. *Magnetohydrodynamics* **44**, 135–142.

ERGIN, F. G., WATZ, B. B., ERGLIS, K. & CEBERS, A. 2010 Poor-contrast particle image processing in micro scale mixing. *Proceedings of the ASME 10th BiennialConference on Engineering Systems Design and Analysis*, pp. 1–5. ASME.

GOYAL, N. & MEIBURG, E. 2006 Miscible displacements in Hele-Shaw cells: two-dimensional base states and their linear stability. *J. Fluid Mech.* **558**, 329–355.

IGONIN, M. 2004 Hydrodynamic instabilities of miscible and immiscible magnetic fluids in a Hele-Shaw cell. PhD thesis, D. Diderot University Paris 7.

IGONIN, M. & CEBERS, A. 2003 Labyrinthine instability of miscible magnetic fluids. *Phys. Fluids* **15**, 1734–1744.

JACKSON, D. P., GOLDSTEIN, R. E. & CEBERS, A. O. 1994 Hydrodynamics of fingering instabilities in dipolar fluids. *Phys. Rev.* E **50**, 298–307.

MAIOROV, M. & CEBERS, A. 1983 Magnetic microconvection on the diffusion front of ferroparticles. *Magnetohydrodynamics* **19**, 376–380.

MEZULIS, A. & BLUMS, E. 2005 Experimental investigations of the microconvective instability in optically induced gratings. *Magnetohydrodynamics* **41**, 341–348.

ROSENSWEIG, R. E. 1985 *Ferrohydrodynamics*. Cambridge University Press.

SAMARSKIJ, A. A. & GULIN, A. V. 1989 *Numerical Methods*. Nauka.

TAN, C. T. & HOMSY, G. M. 1988 Simulation of nonlinear viscous fingering in miscible displacement. *Phys. Fluids* **31**, 1330–1338.

WEN, C.-Y., CHEN, CHING-YAO & KUAN, D.-C. 2007 Experimental studies of labyrinthine instabilities of miscible ferrofluids in a Hele-Shaw cell. *Phys. Fluids* **19**, 084101.

ZIMMERMAN, W. B. & HOMSY, G. M. 1992 Viscous fingering in miscible displacements: unification of effects of viscosity contrast, anisotropic dispersion, and velocity dependence of dispersion on nonlinear finger propagation. *Phys. Fluids* **4** (11), 2348–2359.